Sharp Spatially Constrained Inversion (sSCI)

with applications to transient electromagnetic data

Giulio Vignoli [1], Gianluca Fiandaca [2], Anders Vest Christiansen [2], Casper Kirkegaard [2] and Esben Auken [2]

1 Geological Survey of Denmark and Greenland, Lyseng Allé 1, DK-8270 Højbjerg, Denmark;
formerly at: Hydrogeophysics Group Aarhus University, Department of Geoscience, DK-8000 Aarhus C, Denmark.

2 Hydrogeophysics Group, Aarhus University, Department of Geoscience, DK-8000 Aarhus C, Denmark.

Accepted for publication by *Geophysical Prospecting*

ABSTRACT

Time-domain electromagnetic method data are conveniently inverted for smoothly varying 1D models of fixed vertical discretization. The vertical smoothness of the obtained models stems from the application of Occam type regularization constraints, meant for addressing the ill-posedness of the problem. An important side-effect of such regularization, however, is that horizontal layer boundaries can no longer be accurately reproduced as the model is required to be smoothly varying. This issue can be overcome by inverting for fewer model layers using variable layer thicknesses, but having to decide on a particular and constant number of layers for inversion of a large survey can be equally problematic. Here, we present a focusing regularization technique for getting the best of both methodologies. It allows for accurate reconstruction of resistivity distributions using a fixed vertical discretization, while preserving the capability to reproduce horizontal boundaries. The formulation is flexible and can be coupled with traditional lateral/spatial smoothness constraints, in order to resolve interfaces in stratified soils with no additional hypothesis about the number of layers. The method relies on minimizing the number of layers of non-vanishing resistivity gradient, instead of minimizing the norm of the model variation itself. This approach ensures model results that are consistent with the measured data while favouring, at the same time, horizontal interfaces. The formulation is general and can also be applied in the horizontal direction, in order to promote the reconstruction of lateral boundaries such as faults.

We present the theoretical framework of our regularization methodology and illustrate its capabilities by means of both synthetic and field datasets. We further demonstrate how the concept has been integrated in our existing Spatially Constrained Inversion (SCI) formalism and show its application to large scale time-domain electromagnetic data inversions.

Keywords*: spatially constrained inversion, lateral discontinuities, sharp boundaries, focusing inversion, airborne EM.*

1. INTRODUCTION

Transient electromagnetic (TEM) surveying is a well-established geophysical discipline with applications ranging from mineral exploration to groundwater and geological mapping. A main characteristic of the method is its ability to collect, especially during airborne surveys, extremely large datasets which can be very time consuming to process and invert. Full 3D inversion is possible, but typically impractical due to the size of the surveys. The fact that Maxwell's equations have to be solved for each transmitter location makes the rigorous 3D inversion (e.g., Sasaki 2001; Sasaki 2003) particularly time consuming. Attempts of fast and effective 2D/3D inversion schemes based on approximations have been recently developed and applied to TEM data (Wilson, Raiche and Sugeng 2006; Guillemoteau, Sailhac and Behaegel 2012). With the advent of powerful and inexpensive parallel computers, finite-volume (Haber, Oldenburg and Shekhtman 2007; Yang and Oldenburg 2012), finite-difference (Newman and Commer 2005), and integral equation (Cox, Wilson and Zhdanov 2010) techniques are also becoming increasingly popular and appealing. Up to date, however, 3D inversion is still not near routine practice and for many target settings the benefits of current 3D methods over 1D are still debatable (Viezzoli *et al.* 2010).

Comprehensive TEM inversion codes based on 1D forward modelling typically utilize lateral/spatial constraints to regularize the inversion and obtain solutions that are in accordance with the expected geological variations (Vallée and Smith 2009; Christensen and Tølbøll 2009; Brodie 2010). This approach of inverting for pseudo 2D/3D models, using local 1D models entangled by constraints, has proven very effective in modelling quasi-layered structures where 2D/3D effects are not too pronounced

(Newman, Anderson and Hohmann 1987; Sengpiel and Siemon 2000; Auken *et al.* 2005**).** Most algorithms falling within this category offer support for two types of modelling: "discrete model" inversion that inverts for a limited number of layers with variable layer boundaries, and inversion for "smooth models" based on a large number of stacked layers in a fixed vertical discretization. In the latter case, the inversion problem is typically highly over-determined, making vertical regularization necessary to stabilize the solution (Constable, Parker and Constable 1987). In the former strategy, the inversion can operate without any additional (vertical) regularization, due to its much lower number of free model parameters. Both approaches have their trade-offs, as the smooth one produces sections where formation boundaries are smeared out by regularization, whereas the discrete approach can introduce artefacts in case of unexpectedly complex geology. The discrete model technique is also more sensitive to the specific choice of starting model and for these reasons both types of inversions are typically utilized as tandem complementary solutions.

Here, we describe and demonstrate a novel algorithm that implements an extension of the pseudo 3D formalism Spatially Constrained Inversion (SCI, Viezzoli *et al.* 2008) and its pseudo 2D special case of Laterally Constrained Inversion (LCI, Auken and Christiansen 2004). The extension includes a new regularizing term that is not derived from the L_2 norm of the spatial gradient of the solution, but rather depends on the support of it (Portniaguine and Zhdanov 1999; Zhdanov and Tolstaya 2004; Pagliara and Vignoli 2006; Zhdanov, Vignoli and Ueda 2006; Blaschek, Hördt and Kemna 2008; Vignoli, Cassiani and Deiana 2012). Specifically, we base our new algorithm on gradient support regularization and refer to the full scheme as sharp Spatially Constrained Inversion (sSCI). The introduction of the new regularization term promotes solutions that are both compatible with the observed data and at the same

time features a minimum number of spatial (vertical and/or lateral) model variations. By using this technique we essentially eliminate the need for consulting both discrete and smooth inversions.

2. METHODOLOGY

In the framework of Tikhonov regularization theory (Tikhonov and Arsenin 1977), a priori information is included in the inversion process and formalized via regularizing terms in the objective functional to be minimized. Instead of simply minimizing the distance (usually defined by the L_2 norm) between the observed and calculated data, the regularized objective functional now includes additional stabilizing terms. Hence, the solution minimizing the full objective functional is compatible with both the observed data and any assumptions about the investigated physical system being enforced by the stabilizer. Incorporating a priori information turns the originally ill-posed problem into a well-posed one, where the solution is unique and stable with respect to the data. In particular, we are interested in incorporating the assumption that sharp resistivity changes exist between different lithologies in the investigated subsoil, while the more popular stabilizers promote different features. By far, the most widely used stabilizers are smoothing functionals that constrain the spatial variation of the sought parameter field (Constable *et al.* 1987), which is exactly the kind of regularization employed in the standard SCI algorithm. For SCI, the parameters of neighbouring 1D models are entangled by means of such smoothing regularizing terms, essentially constraining (and smoothing) the amount of spatial variation in the total model space. The SCI scheme further employs vertical regularization on each individual 1D model in the case of inversion for smooth models. With the sSCI formalism, our goal is to resolve layer boundaries by the use of Minimum Gradient Support (MGS) regularization, instead of inverting for discrete models. We investigate the application of MGS along the vertical direction to be able to reconstruct subhorizontal

interfaces, potentially eliminating the need for discrete inversions that make unwanted assumptions about the ground layering. For the horizontal direction, we apply the sSCI approach to effectively resolve lateral discontinuities due to e.g. faults or blocky mineral inclusions.

2.1 ALGORITHM: FROM SCI to sSCI

Spatially and laterally constrained 1D inversion techniques have been successfully applied to many different kinds of data including vertical electrical soundings (Auken and Christiansen 2004; Auken *et al.* 2005), seismic surface wave (Wisén and Christiansen 2005), transient electromagnetics (Auken *et al.* 2008; Viezzoli *et al.* 2008), frequency-domain electromagnetics (Monteiro Santos 2004; Brodie and Sambridge 2006; Triantafilis and Monteiro Santos 2009), magnetic resonance soundings (Behroozmand *et al.* 2012b) and time domain induced polarization (Fiandaca *et al.* 2012, Fiandaca *et al.* 2013). For simplicity, we consider the special case of SCI inversion of TEM data. In this case, the vectors in the data and in the model space respectively become:

$$\mathbf{d} = \left[\log(\rho_{a1}),\quad \log(\rho_{a2}),\quad \log(\rho_{a3}),\quad \ldots,\quad \log(\rho_{aN})\right]^T, \tag{1}$$

and

$$\mathbf{m} = \left[\mathbf{m}_1,\quad \mathbf{m}_2,\quad \mathbf{m}_3,\quad \ldots,\quad \mathbf{m}_{n_x}\right]^T. \tag{2}$$

In these equations ρ_{ai}, $i = 1,\ldots,N$ denotes the apparent resistivity data collected along a profile and for different time gates, and each $\mathbf{m}_j$, $j = 1,\ldots,n_x$ is the vector of the n_ℓ resistivities and the $(n_\ell - 1)$ thicknesses at the *j-th* sounding position: $\mathbf{m}_j = \left[\log(\rho_{j1}), \ldots, \log(\rho_{jn_\ell}), \log(t_{j1}), \ldots, \log(t_{j(n_\ell-1)})\right]^T$.

Thus, the estimated solution is the minimizer of the summation between the data misfit

$$\phi(\mathbf{m}) = \left\| \mathbf{Q}_d \ \ (\mathbf{d}_{obs} - g(\mathbf{m})) \right\|_{L_2}^2 \tag{3}$$

and the stabilizer terms in the form of

$$s(\mathbf{m}) = \left\| \boldsymbol{\beta}^{-1} \ \mathbf{Q}_p \ \mathbf{R}_p \ \ \mathbf{m} \right\|_{L_2}^2 ; \tag{4}$$

where, g is the nonlinear mapping relating the model to the data space, $\mathbf{R}_p$ is the roughness operator providing the specifics of the regularization, and $\boldsymbol{\beta}^{-1}$ consists of a diagonal matrix of weights controlling the relative importance between the data and the stabilizer. Finally, $\mathbf{Q}_\mathrm{p}$ and $\mathbf{Q}_\mathrm{d}$ are simple weighting matrices in the model and data space, respectively. In the data case $\mathbf{Q}_\mathrm{d}$ typically weights the data residuals by the inverse of the uncertainty in the data:

$$(\mathbf{Q}_d)_i = \delta_i^{-1} . \tag{5}$$

About the specifics of the introduced properties, in the original LCI/SCI schemes (e.g., Auken and Christiansen 2004; Viezzoli *et al.* 2008), the roughness matrix $\mathbf{R}_\mathrm{p}$ is implemented as a linear difference operator and the entries of the diagonal $\boldsymbol{\beta}$ matrix are all set to unity; in the case of $\mathbf{Q}_p$, the entries simply specify the different degrees of variability associated with the constraints.

Having defined the equations of the inversion problem, we minimize the non-linear objective function using the Levenberg-Marquart algorithm, providing a solution by iterating over *n*:

$$\mathbf{m}_{n+1}^{(\mathrm{SCI})} = \mathbf{m}_n^{(\mathrm{SCI})} + \left\{ \begin{bmatrix} \mathbf{G}_n^T \mathbf{C}_{obs}^{-1} \mathbf{G}_n + \dfrac{1}{\beta} \mathbf{R}_p^T \mathbf{C}_c^{-1} \mathbf{R}_p + \lambda \mathbf{I} \end{bmatrix}^{-1} \cdot \begin{bmatrix} \mathbf{G}_n^T \mathbf{C}_{obs}^{-1} \left(\mathbf{d}_{obs} - \mathrm{g}(\mathbf{m}_n^{(\mathrm{SCI})}) \right) + \dfrac{1}{\beta} \mathbf{R}_p^T \mathbf{C}_c^{-1} \left(- \mathbf{R}_p \mathbf{m}_n^{(\mathrm{SCI})} \right) \end{bmatrix} \right\}, \tag{6}$$

where, $\mathbf{G}_n$ is the Jacobian matrix of the nonlinear mapping g, $\mathbf{C}_{obs}^{-1} = \mathbf{Q}_d^T \mathbf{Q}_d$ is a covariance matrix specifying the data uncertainties, while $\mathbf{C}_c^{-1} = \mathbf{Q}_p^T \mathbf{Q}_p$ specifies the strength of the regularizing constraints, and λ is simply a Marquart damping parameter that is iteratively updated to stabilize the minimization process (Marquart 1963).

The reason of the SCI smoothness is clear if we rewrite Equation (4) in a more explicit way:

$$s^{(SCI)}(\mathbf{m}) = \frac{1}{\beta} \sum_k \frac{(\mathbf{R}_p \mathbf{m})_k^2}{\sigma_k^2}, \tag{7}$$

In minimizing the stabilizer, the contribution $(\mathbf{R}_p \mathbf{m})_k^2 / \sigma_k^2$ of the *k-th* term, which will be referred to as a "penalization" term, is proportional to the square of the value of the variation of the *k-th* component of $\mathbf{m}$. This linear relationship is illustrated with a straight line in Figure 1, which clearly shows that an increase in model parameter variation will always lead to greater penalization in the stabilizer. This intrinsic property of the minimum L_2 norm methodology essentially prevents reconstruction of blocky features, as we will show that this requires an upper limit on the degree of penalization regardless of variation magnitude. To overcome this issue, for the sSCI implementation, we use a MGS stabilizer weighted by the model variances. The full expression for this stabilizer is shown in Equation (8):

$$s^{(sSCI)}(\mathbf{m}) = \sum_k \frac{1}{\beta_k} \frac{\left(\frac{(\mathbf{R}_p \mathbf{m})_k}{\sigma_k} \right)^2}{\left(\frac{(\mathbf{R}_p \mathbf{m})_k}{\sigma_k} \right)^2 + \varepsilon^2}, \tag{8}$$

and in the following we discuss its properties.

Within the formalism of the sSCI, we use the model variance σ_k as a tuneable threshold controlling the sharpness of the inversion, while we keep the ε parameter constant. To explain the reasoning behind this, we first discuss how we select the value for ε from the plot in Figure 1 showing the variability of the sSCI norm as a function of the weighted model variation, for different ε^2 values. When $\varepsilon^2 = 1$, σ_k acts as a loosely defined threshold: model variations with $\left(\frac{(\mathbf{R}_p \mathbf{m})_k}{\sigma_k} \right)^2 < 1$ are weakly penalized, while model variations above σ_k can never contribute with a penalization larger than one. Hence, by using an MGS stabilizer with $\varepsilon^2 = 1$, we penalize only the number of variations larger than the threshold, rather than the magnitude of the variation itself. Moreover, the use of $\varepsilon^2 = 1$ provides the benefit of obtaining similar behaviour for the MGS stabilizer and the L_2 norm stabilizer for small values of $(\mathbf{R}_p \mathbf{m})_k^2 / \sigma_k^2$ (Figure 1). This allows for reconstruction of sharp boundary targets while maintaining the effect of smoothing regularization for small model parameter variations. By selecting too small ε^2 values (in Figure 1, $\varepsilon^2 = 0.05$ and 0.02), we basically apply the same, maximum, penalization to every model characterized by a variation different from zero. This would result in a very oscillating solution since it does not really matter if the variation is large or small as long as it is non-zero. On the contrary, if a large ε^2 value (e.g., $\varepsilon^2 = 10$) is used, a penalization nearly proportional to the model variation is applied. And, in this case, the regularization will not lead to the desired blocky solution.

Thus, σ_k defines the threshold where a model parameter variation is considered large enough to be penalized (i.e., it is large enough to contribute to the focusing MGS stabilizer in the Equation (8) and Figure 1). In another words, σ_k, and the corresponding $\mathbf{C}_c$ entries, define the level of homogeneity in each reconstructed sub-volume, and the level of (non-penalized) variability within each different area.

Basically, by setting σ_k equal to, for example, 1.04, the MGS stabilizer will count as possible variations all the resistivity changes larger that 4%; hence, all the structurs with a variability within 4% will be considered homogeneous.

Concerning the diagonal matrix $\boldsymbol{\beta}$, we use only two distinct values for its entries. One value for the entries in Equation (8) involving the vertical variation and another for the horizontal components. In general, the $\boldsymbol{\beta}$ matrix elements control the balance between data misfit and regularization and therefore they should be chosen to fit the data to an appropriate degree. For the sSCI, however, the use of two distinct values of $\boldsymbol{\beta}$ extends its functionality to further control the ratio between horizontal and vertical focusing strength. In the following, for the sSCI we set the two $\boldsymbol{\beta}$ component values to 15 normalized, respectively, for the number of lateral, and vertical constraints per 1D model. We choose these values on the basis of a large number of numerical experiments that demonstrate these numbers to be robust and not requiring significant adjustments. In general, by selecting smaller numbers for $\boldsymbol{\beta}$ we could obtain more blocky solution, but without achieving the desired data misfit. On the other hand, too large $\boldsymbol{\beta}$ component values leaded to smoother solutions.

We now discuss a straight forward way to integrate the novel sSCI regularization into the existing SCI minimization scheme. The smoothing functional in Equation (7) uses the L_2 norm of the model variation $\mathbf{R}_p\mathbf{m}$ and the only difference with the sharp functional in Equation (8) is in the weighting matrix. In the former case the weighting matrix is the diagonal matrix of the model variances, whereas in the latter case the weighting matrix simply becomes: $\mathbf{Q}_p^{(sSCI)} = \mathbf{W}_\varepsilon \mathbf{Q}_p^{(SCI)} \mathbf{R}_p = \mathbf{Q}_p^{(SCI)} \mathbf{H}_\varepsilon$. Where, $\mathbf{W}_\varepsilon$ is a diagonal matrix with non-zero elements equal to

$$(\mathbf{W}_\varepsilon)_k = \frac{1}{\sqrt{(\mathbf{Q}_p^{(SCI)}\,\mathbf{R}_p\,\mathbf{m})_k^2 + \varepsilon^2}}. \qquad (9)$$

From this expression, we see that the introduction of the sharp MGS stabilizer has made the weighting matrix elements model dependent (Vignoli *et al.* 2012). In principle, in the iterative model update expression, terms containing the Fréchet derivative of $\mathbf{W}_\varepsilon$ with respect of $\mathbf{m}$ should be included. Examples of inversion algorithm based on the minimum support stabilizer and taking into account these terms are described in Zhdanov *et al.* (2006) and Vignoli *et al.* (2012). However, since we wanted to implement a focusing algorithm by introducing the minimum number of modifications with respect to the original SCI scheme, we disregard those terms and use instead a re-weighting strategy taking into account simply the terms with $\mathbf{W}_\varepsilon$. Thus, the variable weighting matrix $\mathbf{W}_\varepsilon$ is recomputed on each iteration $\mathbf{W}_\varepsilon = \mathbf{W}_\varepsilon^{(n)} = \mathbf{W}_\varepsilon(\mathbf{m}_n)$ based on the $\mathbf{m}_n$ from the previous iteration, while the contributions of the terms accounting for the derivative of $\mathbf{W}_\varepsilon$ are neglected. This simplified approach leads to an iterative model update expression for the sSCI that is extremely close to the Equation (6) concerning the SCI:

$$\mathbf{m}_{n+1}^{(\mathrm{sSCI})} = \mathbf{m}_n^{(\mathrm{sSCI})} + \left\{ \begin{array}{l} \left[\mathbf{G}_n^T \mathbf{C}_{obs}^{-1} \mathbf{G}_n + \boldsymbol{\beta}^{-1} (\mathbf{H}_\varepsilon^{(n)})^{\mathrm{T}} \mathbf{C}_c^{-1} \mathbf{H}_\varepsilon^{(n)} + \lambda \mathrm{I}\right]^{-1} \cdot \\ \left[\mathbf{G}_n^T \mathbf{C}_{obs}^{-1} \left(\mathbf{d}_{obs} - \mathrm{g}(\mathbf{m}_n^{(\mathrm{sSCI})})\right) + \boldsymbol{\beta}^{-1} (\mathbf{H}_\varepsilon^{(n)})^{\mathrm{T}} \mathbf{C}_c^{-1} \left(-\mathbf{H}_\varepsilon^{(n)} \mathbf{m}_n^{(\mathrm{sSCI})}\right)\right] \end{array} \right\} \qquad (10)$$

In summary, the inversion algorithm for sSCI is the same as for SCI after substituting the (constant) roughness operator $\mathbf{R}_p$ with the matrix (updated iteration by iteration) $\mathbf{H}_\varepsilon^{(n)}$.

In principle, neglecting the terms containing the $\mathbf{W}_\varepsilon$ derivative could lead to convergence issues in the minimization, however, we have not experienced any problems in practice. For the re-weighted optimization used here, the convergence rate depends on how accurate the (pseudo-quadratic)

approximation of the weighting matrix $\mathbf{H}_{\varepsilon}^{(n)}$ is with respect to the original (non-quadratic) norm (Zhdanov 2002). Across all of our numerical experiments, we find that the convergence rate of the SCI algorithm remains essentially the same even after adding the sSCI term.

3. SYNTETIC DATA

We demonstrate the application of the new algorithm by using two synthetic examples. In particular, we compare the capabilities of the sSCI in reproducing layer boundaries against the smooth and discrete SCI inversions. The goals are to assess whether sSCI can be adopted as a valid alternative to discrete inversions and understand the differences between sSCI and traditional smooth SCI.

The considered synthetic models are representative structures of typical glacial buried valleys. Buried valleys are complex structures filled with glacio-lacustric clay, till, meltwater sand and gravel that provide classical target structures for hydrogeophysical surveys. The presented models mimic those discussed by Jørgensen *et al.* (2012) and the details of generating the synthetic 3D TEM data using the TEMDDD code (Árnason 2008) are the same as discussed by Auken *et al.* (2008). Both synthetic models are characterized by a 3D resistivity distribution, where the top layer of the model represents soil of varying randomly generated resistivity. Located beneath the top layer, we find the actual 2D buried valley structures themselves. The synthetic data extracted from the models provide a simulation of a ground-based TEM instrument, transmitting a 3 A current in a 40 m x 40 m square loop. This data were perturbed by noise consisting of: 1) Gaussian 2% contribution, and 2) "background" contribution characterized by a $t^{-1/2}$ trend with a value of 3 nV/m^2 at 1 ms (Auken *et al.* 2008). Having applied the noise perturbation, the synthetic data were processed as any field dataset, resulting in an uneven number of gates per sounding and varying error bars. For the inversion itself, a uniform half-space of 50 Ωm was used for the

starting model, using logarithmically increasing layer thicknesses for the vertical discretization. Spatial regularization was applied using constant setting throughout all inversions and applied to the resistivity values. For the smooth horizontal regularization, a constraint factor of 1.2 was used for entangling resistivities of neighbouring model layers and, for the smooth vertical direction, we used a factor of 2.0. As the inversion is performed in logarithmic model space, these values essentially amount to assigning a variance of ~20% on the resistivities of horizontally neighbouring layers and a variance of ~100% in the vertical direction. For the sSCI, we use the global constant settings presented in the previous section, amounting to $\sigma_k = 1.04$ and $\sigma_m = 1.12$ (here, the *k* and *m* indexes are respectively spanning the $\mathbf{C}_c$ components concerning the horizontal and vertical constraints). Thus, by using these values, the regularization essentially considers an area homogenous when the horizontal and vertical variations are smaller than 4% and 12%, respectively.

3.1 Model A

A section of the first discussed synthetic model is shown in Figure 2. It is a relatively simple valley (Figure 2a) incised into thick clays (5 Ωm) and filled by sands below the groundwater table (100 Ωm). The valley has 26^o sloping flanks with the bottom situated at a depth of 150 m. The top layer is inhomogeneous with a log-normal resistivity distribution having a mean value of 40 Ωm for the left side (clay-till) and 400 Ωm, for the right side (dry sandy quaternary layer).

Comparing the final inversion model, we find the 16-layer smooth SCI result (Figure 2b) to retrieve reasonably well the main features of the true model: the mean resistivity value of the top layer is well reconstructed on both sides, the resistivity of the valley is slightly overestimated (especially on the left side), while the flanks appear less steep than they actually are due to the presence of a smooth (artificial)

transition between the (overestimated) high resistivity inside the valley and the conductive clay. When MGS constraints are applied along the vertical direction, while utilizing regular SCI smoothing laterally, the quality of the final result somewhat improves (Figure 2c). The resistivity level of the valley fill is now slightly better determined and also more homogeneously reproduced (even if the resistivity of the left side of the valley is still higher that the true value). The boundary at the interface between the first layer and the valley is more precisely retrieved. For example, the artificial horizontal transition at the bottom of the first layer, on the right side, introduced by the smooth inversion (Figure 2b) has been almost completely removed by the vertical sharp algorithm (Figure 2c).

The sSCI using MGS constraints in both the vertical and horizontal direction (Figure 2d) further improves the result. Not only the actual locations of the abrupt resistivity changes in the true model are more accurately mapped (e.g., the interface between the first layer and the sandy valley along the entire section is precisely located), but the true resistivity values are also more correctly recovered. For example, the sand homogeneous resistivity is very well inferred almost to the depth of investigation (DOI - Christiansen and Auken 2012). Clearly, the MGS algorithm enhances all the "sharp" features in the data, including the, so-called, "pant-leg" effect due to presence of an abrupt, lateral change in conductivity. Hence, for example, the vertical boundary in the top layer results in a spurious conductive feature in the first few tens of metres in the valley fill. This artefact is present in all the reconstruction in Figure 2, but is less fuzzy and more clearly detectable in the sharp reconstructions.

3.2 Model B

The second synthetic example consists of a 20 Ωm body embedded a more conductive half-space, and filling the right side base of a paleovalley (Figure 3a) characterized, on the left side, by a 100 Ωm resistivity. The top layer now consists of a single mean resistivity value of 40 Ωm for a single log-normal

resistivity distribution across the whole area. Comparing the inversion results, we again find that the standard smooth SCI is fairly successful in recovering the overall picture (Figure 3b). If, instead of 16, only 4 layers are used for a laterally smooth SCI, the result in Figure 3c is obtained. A 4-layers parameterization has been chosen since the true model is characterized by 4 layers. In this inversion, no vertical constraints are connecting the resistivity values within each 1D model and simply the usual lateral smoothness is enforced ($\sigma_k = 1.2$). The most evident difference between Figure 3b and Figure 3c is in the higher precision of the few-layer inversion in locating the interfaces defining the resistive layers and the depth of the resistive valley. Also the flanks of the conductive valley are better resolved since the few-layer parameterization contributes to get rid of the smearing effect due to the smooth regularization. Similarly to Figure 3b, the bottom of the conductive valley cannot be resolved since it is at the upper DOI limit.

In case of sSCI utilizing vertical and horizontal MGS constraints (Figure 3d), we again find that the reconstruction is significantly improved: the location of interfaces is more accurate and the overall resistivity levels are better recovered without over-shooting the resistivity of the shallower valley. The result in Figure 3d confirms that sSCI inherits, at the same time, the advantages of the multi-layer (regularized) inversion and the discrete (few-layer) reconstruction, thus, allowing retrieving the resistivity distributions by means of a fixed vertical discretization, while preserving the capability to reproduce sharp features. In particular, the two 70 Ωm structures between 30 and 75 m depth are quite well retrieved both in terms of boundary location and resistivity value. The flanks of the resistive valley are reconstructed to a level comparable to the few-layer inversion quality.

Clearly, all the regularization schemes we have used are designed to penalize, in different ways, the lateral resistivity variation. And, when the sensitivity of the physical method is not high enough, it might

happen that the contribution from the stabilizing term is predominant. Hence, the information migrates from the areas better constrained by the data to the others. This explains why the bottom of the resistive valley embedded in a more conductive medium is hard to be correctly recovered and why, in all reconstructions, the valley base appears to be less resistive than in the true model. Of course, like for the "pant-leg" effect in Model A, also for the Model B, when the sSCI algorithm is used, the regularization artefact are sharper, and so, somewhat more pronounced.

4. FIELD DATA

As part of the CLIWAT project (Harbo *et al.* 2011), airborne TEM data were collected near Tønder in southern Denmark in April 2009 (Figure 4). The aim of the survey was to obtain a better understanding of the geological and hydrogeological setting of the area, in particular by mapping buried valleys and salt-fresh water interfaces (Jørgensen *et al.* 2012). The dataset was acquired using the SkyTEM system (Sørensen and Auken 2004) operating at an average speed of 43 km/h for a resulting averaged sounding every 25-30 m. Processing of the data was done using the methodology of Auken *et al.* (2009), as implemented in the Aarhus Workbench software package (www.aarhusgeophysics.com).

In order to best assess the differences between sSCI and SCI for actual field data, we show results for two very characteristic cross-sections. The first is characterized by sharp lateral and vertical variations in the resistivity distribution (probably a fault), and the second is well suited for comparison due to the existence of high quality borehole information close to the geophysical section.

Figure 5 and Figure 6 show the results of the respective 30-layer SCI and sSCI inversions, all performed using the same settings as in the synthetic cases.

The geology of the area consists mainly of three sedimentary sequences: alternating Miocene sand, silt and clay layers overlying Paleocene clay situated at about 300 m depth. The Miocene sequence is found

below a shallow sheet of coarse glacial meltwater sediments and tills, which occasionally thickens when a buried valley is being filled. The inversions of the first cross section are shown in Figure 5. Both inversion results achieve the same degree of data fit. In the southern part of the cross section, we find a fault located at around 5250 m, providing a very interesting target for comparison. Here, we see that the focusing regularization of the sSCI effectively eliminates transition zone effects and provides a sharper and much more realistic result. Along the entire section, in the smooth SCI inversion, we can notice two thin layers of slightly increased resistivity surrounding the conductive layer (Figure 5a), while these layers do not exist in the focusing sSCI inversion (Figure 5b). The sSCI solution of Figure 5b provides (with a comparable data misfit) a much simpler picture characterized by a few, very homogeneous, zones that are much easier to interpret by a geologist. This prospect is of particular interest when looking towards future automated methods for relating geophysical- and hydrological/lithological models (http://geofysiksamarbejdet.au.dk/en/hygem/project-description/).

About the second field data example, as seen in Figure 6, we compare the SCI and sSCI results against a borehole located just a few meters from the cross section (Figure 4). By comparing the inversion results to ground truth, it is clear that the sSCI (Figure 6b) is capable of reproducing the actual lithological transitions with much higher precision than the smooth SCI. In particular, it is hard to tell from the smooth SCI whether there are two distinct layers above the Miocene clay or if this is just a single smeared out interface. In the sSCI case, two completely unambiguous layers are revealed, providing an almost perfect reconstruction of the interface between the top sand/gravel layer and the underlying clay. For the deeper lying layers the sSCI again provides an excellent definition of the Miocene clay between -30 and -52m and its transition to a sandier lithology from -52m down to the depth of investigation. As a matter of fact, sSCI also appear successful in determining the sharp change to the sand layer situated immediately above the depth of investigation (Figure 6b).

5. CONCLUSIONS

In this paper we have developed and applied an extension of the regularization used in the Spatially Constrained Inversion scheme (SCI). The new sharp SCI algorithm (sSCI) implements a Minimum Gradient Support (MGS) stabilizer as a simple extension of the existing SCI scheme, i.e. essentially adding just a new model-vector dependent contribution to the regularization term. The new focusing stabilizer allows for the reconstruction of abrupt horizontal variations without turning to discrete inversions for variable layer boundaries, while at the same time offering also support for improved reconstruction of horizontal interfaces. The application of the new methodology significantly extends the applicability of the local 1D formulation of the SCI, as the sSCI now supports transitions between different quasi layered sub-settings and provides improved support for mapping of discrete structures. The improved algorithm is very easy to be implemented and is proven to be effective on both synthetic and field TEM data sets. In the synthetic examples we show how the sSCI compares to the traditional smooth and discrete SCI; the synthetic examples clearly demonstrate the sSCI superior capability to resolve abrupt resistivity changes. In the case of actual field data, sSCI produces results that are much more geologically plausible, more homogeneous and also retrieves more accurately the lithological information obtained from a borehole.

Overall, we draw the conclusion that, in quasi-layered settings, it is beneficial to employ a custom regularization scheme, such as sSCI, instead of simply utilizing one of the more widely known smoothing stabilizers. Specifically, the sSCI provides the benefit of making no assumptions about a fixed number of layers in the ground, which is otherwise needed in order to resolve sharp resistivity variations by inverting for models of variable layer boundaries. Another intriguing feature of the sSCI approach is its ability to produce a quasi 3D model made up from subdomains of (quasi-)homogeneous resistivity. This

capability could prove highly valuable for applications requiring models of minimum detail, e.g. automated geological interpretation schemes or integration with hydrological models.

The novel focusing algorithm is independent on the specific spatial derivative operator used. Thus, it can be coupled with no additional modifications to sophisticated $\mathbf{R}_p$ implementations. This might be useful, for example, anytime the subsurface stratification does not follow the surface; in these cases, a derivative implementation that is taking into account, not simply the contributions from model parameters at the same depth, but also contributions along the "diagonal" directions could prevent the layers to be incorrectly forced to follow the surface.

Concerning future applications, we have implemented the formalism in a general and flexible way, that makes it very easy to apply the methodology to other data types. In fact, the presented sSCI scheme could be useful for any problem utilizing a 1D forward model for the purpose of resolving sharp variations in either the horizontal or vertical direction. Examples of this could be: 1) the inversion of seismic surface wave data, anytime the dispersion curves are extracted via techniques preserving information about rapid lateral transition (Vignoli and Cassiani 2010; Vignoli *et al.* 2011), and 2) application to the case of adjacent magnetic resonance soundings (Behroozmand *et al.* 2012a).

6. ACKNOWLEDGEMENTS

The authors acknowledge the World Bank and the Indian Government, Ministry of Water Resources, for their partial support to this research within the framework of the Aquifer Indian Mapping (AQUIM) project (http://geofysiksamarbejdet.au.dk/en/projects/aquim/). Especially, they would like to thank Dr. Shakeel Ahmed and Dr. Subash Chandra from the Indian National Geophysical Research Institute. We

also thank the VILLUM center of excellence HOBE for their partial support. Moreover, the authors are grateful to the two anonymous reviewers for their valuable suggestions.

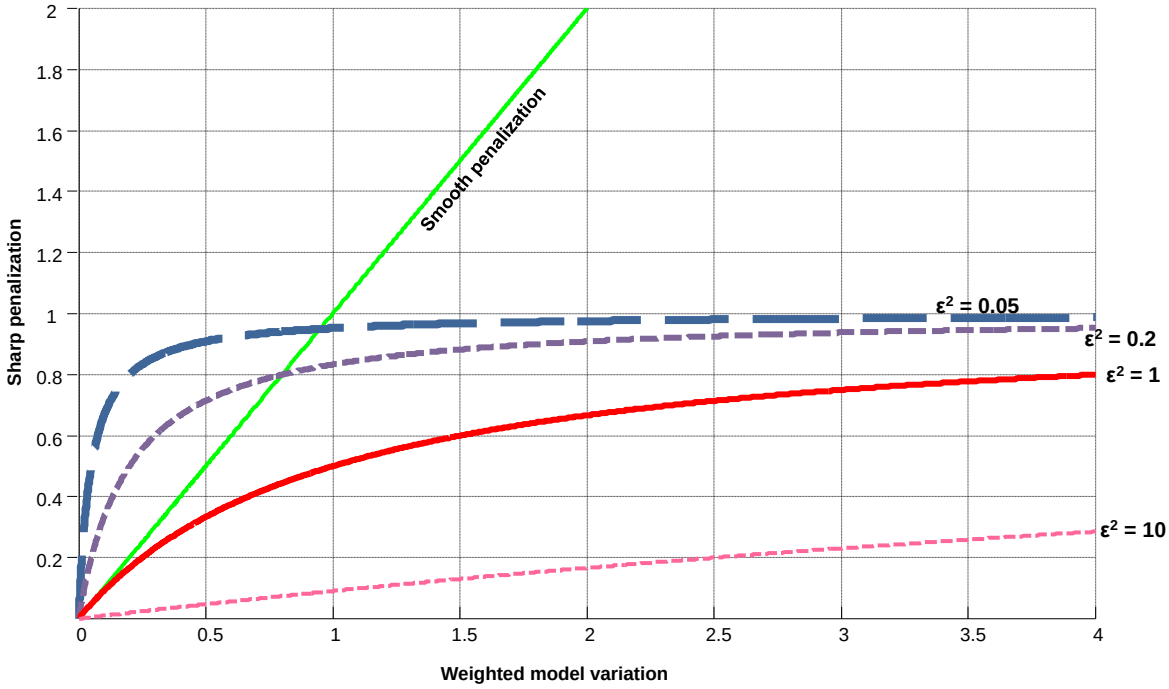

Figure 1: Sharp penalization $\left(\frac{(\mathbf{R}_p\mathbf{m})_k}{\sigma_k}\right)^2 \Big/ \left[\left(\frac{(\mathbf{R}_p\mathbf{m})_k}{\sigma_k}\right)^2 + \varepsilon^2\right]$ plotted against the weighted variation of the model $\left(\frac{(\mathbf{R}_p\mathbf{m})_k}{\sigma_k}\right)^2$ for different values of the focusing parameter ε^2. For comparison the smooth penalization $\left(\frac{(\mathbf{R}_p\mathbf{m})_k}{\sigma_k}\right)^2$ is also shown (solid green line).

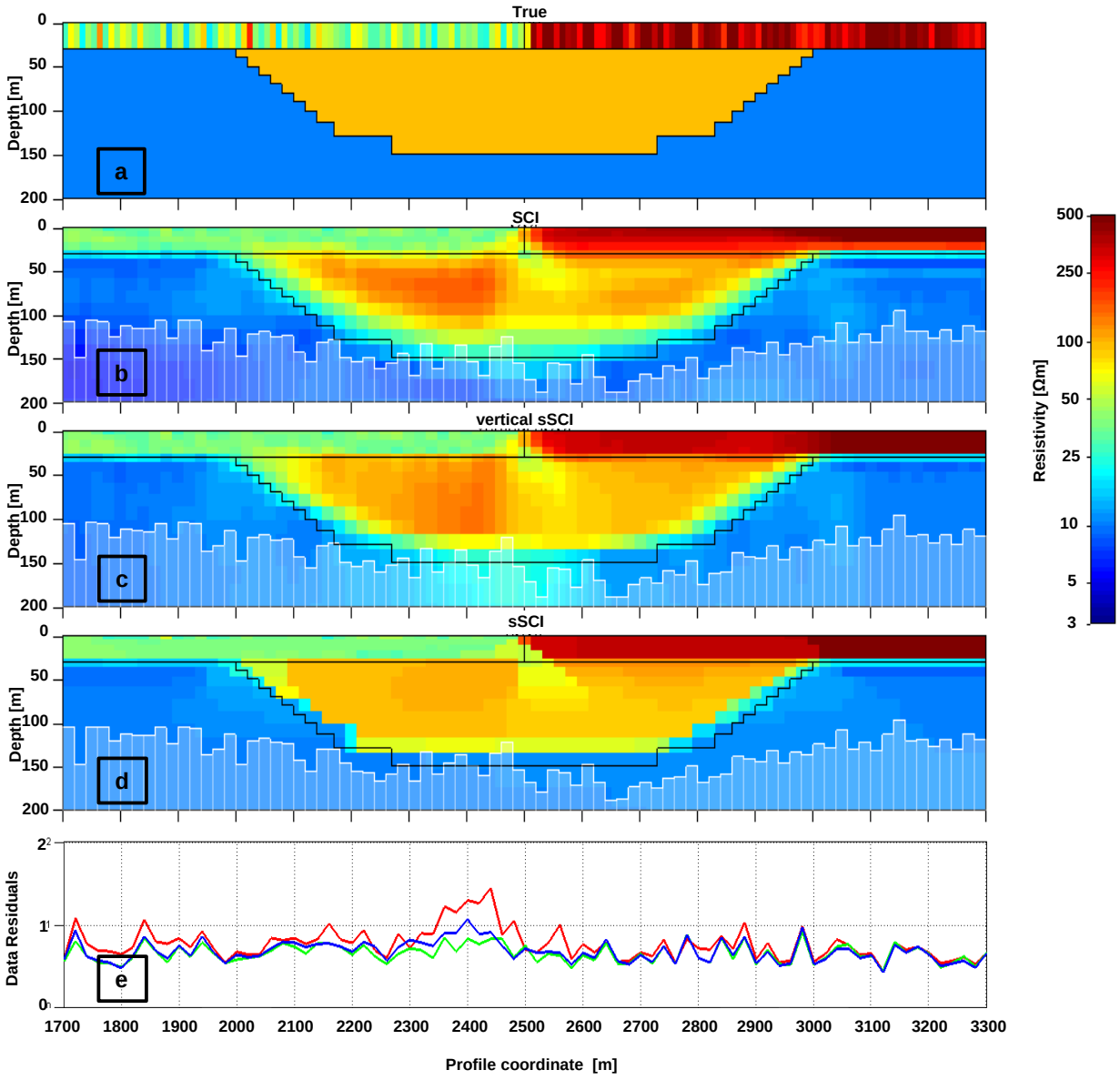

Figure 2: Model A. a) True model. b) SCI result (smooth constraints both in vertical and horizontal direction). c) Vertical sSCI (laterally smooth and vertically sharp constraints). d) sSCI (sharp constraints both in vertical and horizontal direction). e) Data misfit: green, blue and red lines, show, respectively, the residuals for the SCI, vertical sSCI, and multidirectional sSCI. The white-shaded area represents the depth of investigation (DOI). Vertical exaggeration = 1.6x.

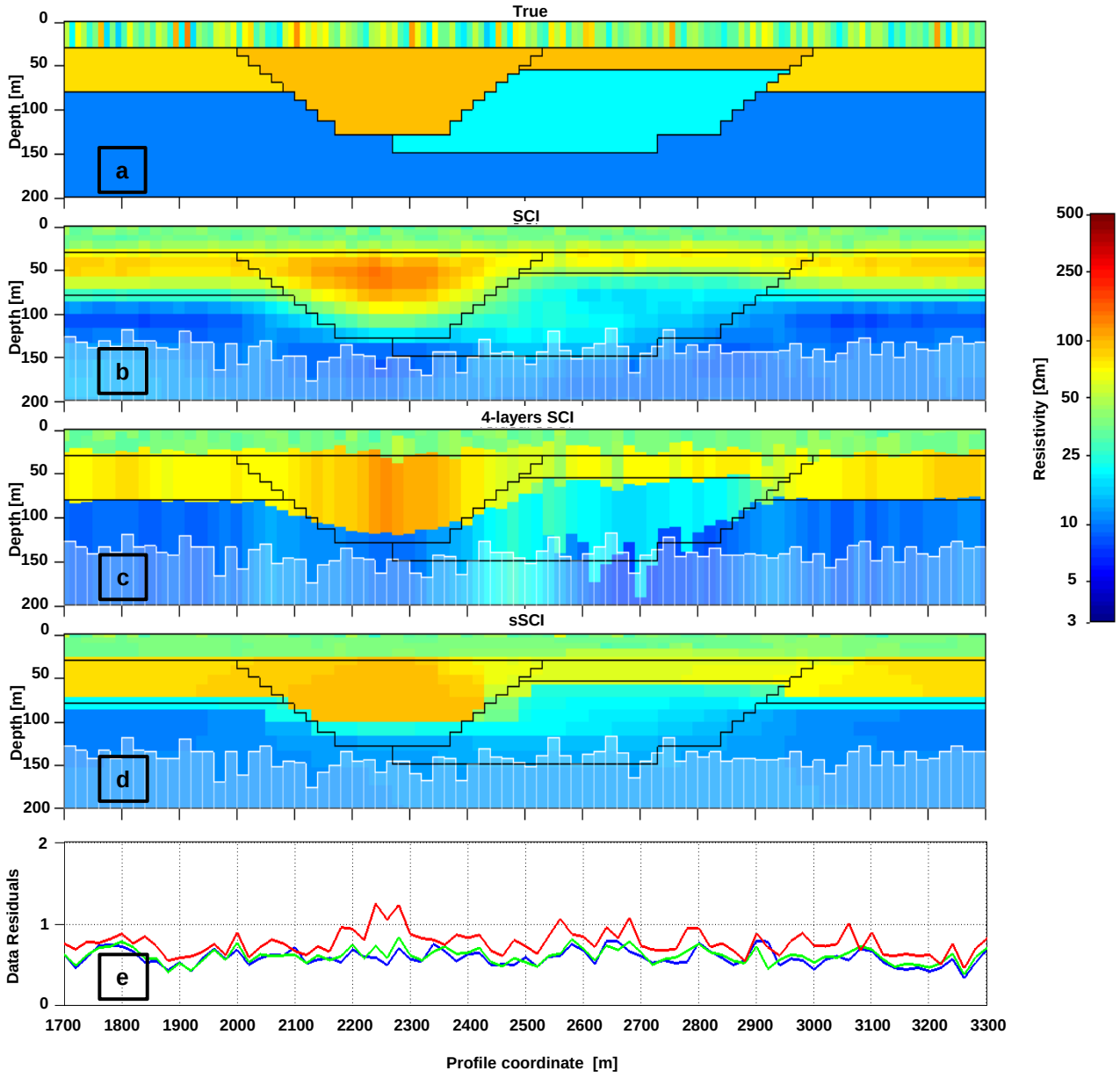

Figure 3: Model B. a) True model. b) SCI result (smooth constraints both in vertical and horizontal direction). c) Discrete SCI (laterally smooth with a few-layer parameterization). d) sSCI (sharp constraints both in vertical and horizontal direction). e) Data misfit: green, blue and red lines, show, respectively, the residuals for the multilayer SCI, few-layer SCI, and multilayer sSCI. The white-shaded area represents the DOI. Vertical exaggeration = 1.6x.

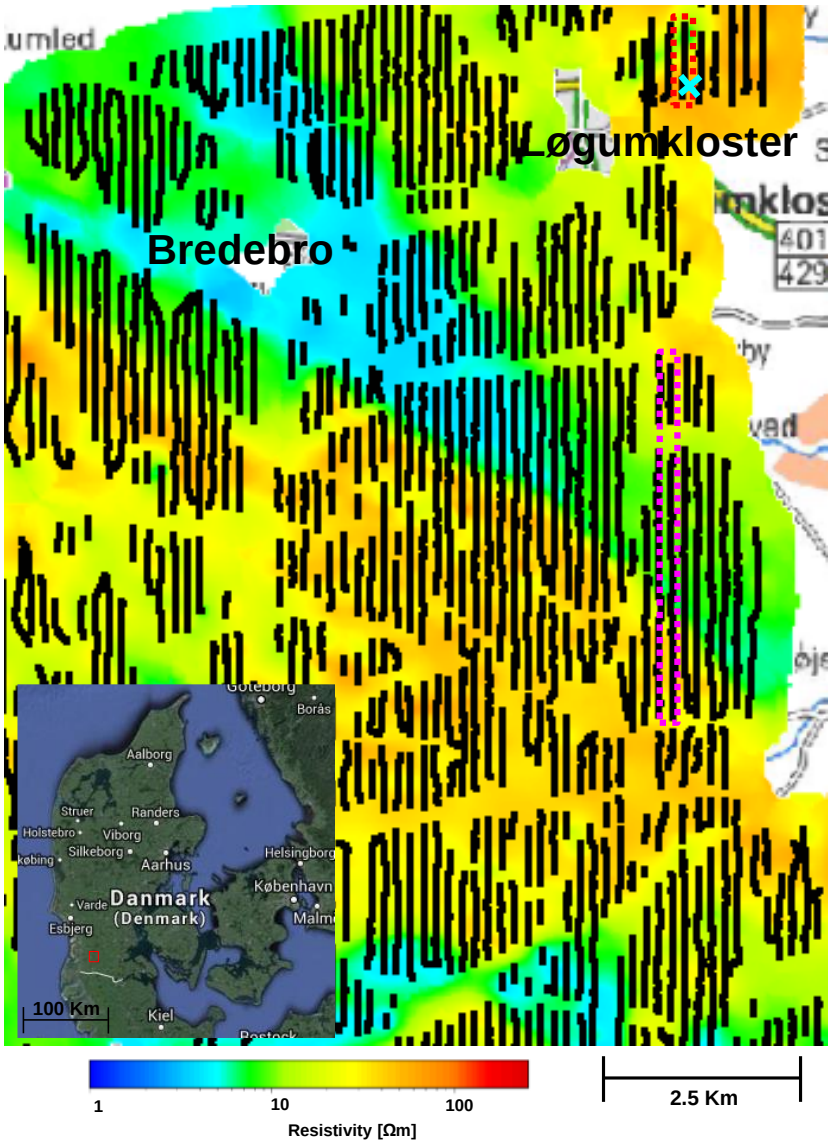

Figure 4: Map of the mean resistivity between -70 and -80 m elevation of the survey area located near the border of Germany and Denmark. The sounding locations are shown in black (sounding characterized by capacitive/galvanic couplings and/or not optimal acquisition parameters have been removed). The two considered survey portions are inside the dash rectangles: in violet the section in Figure 5, in red the one in Figure 6. The blue cross marks the location of the borehole used for comparison in Figure 6.

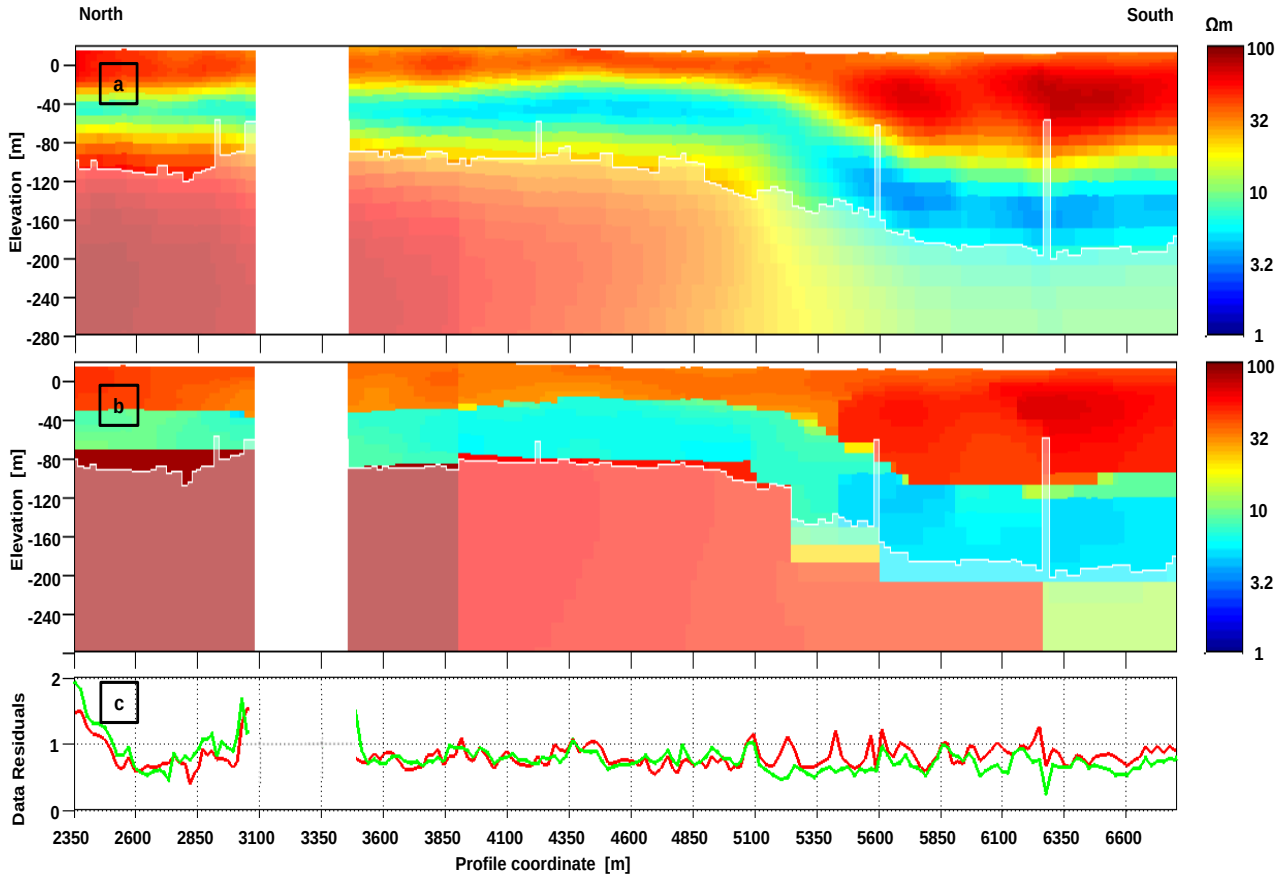

Figure 5**:** Southern cross section. a) SCI. b) sSCI. c) Data misfit at each sounding location; the green and red lines represent the misfit of the SCI and the sSCI, respectively. The white-shaded area represents the DOI. Vertical exaggeration = 3.4x.

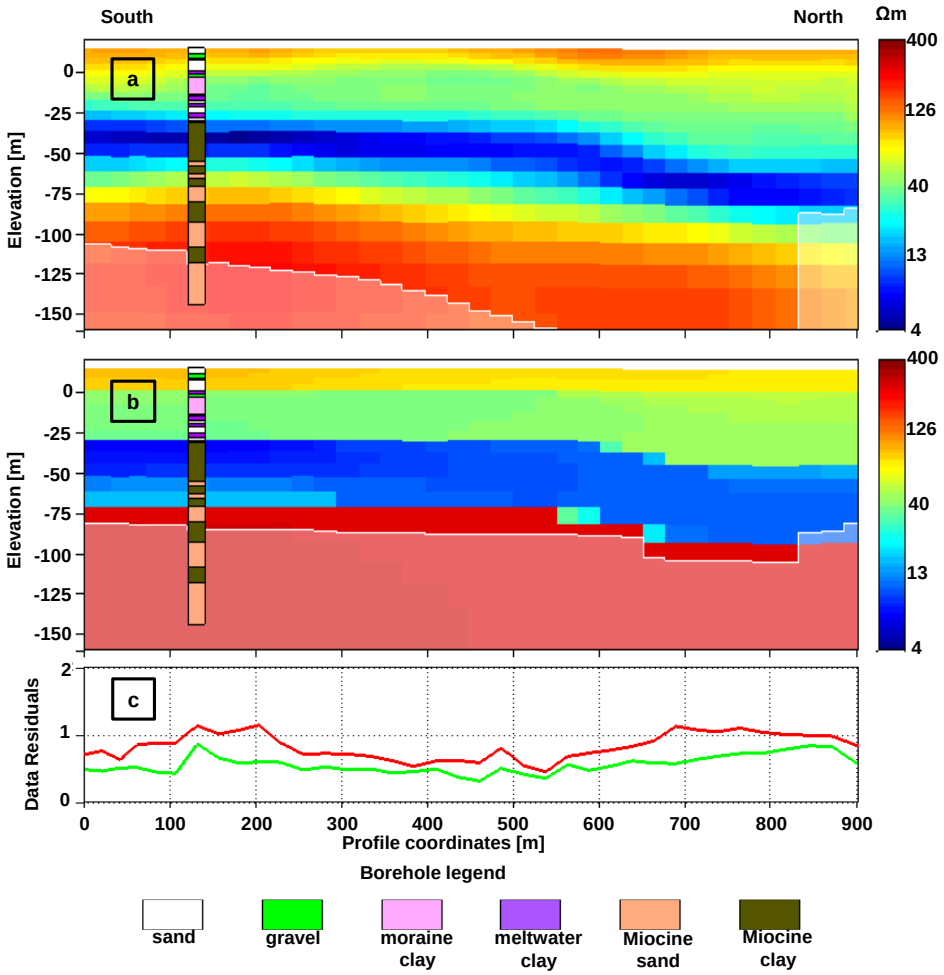

Figure 6: Northern cross section. a) SCI and b) sSCI resistivity results compared against the available borehole. c) Data misfit at each sounding location; the green and red lines represent the misfit of the SCI and the sSCI, respectively. The white-shaded area represents the DOI. Vertical exaggeration = 1.9x.

Reference List

1. Árnason K. 2008. A short Manual for the program TEMDDD. The National Energy Authority of Iceland, Reykjavík, Iceland.
2. Auken E. and Christiansen A.V. 2004. Layered and laterally constrained 2D inversion of resistivity data. Geophysics 69, 752-761.
3. Auken E., Christiansen A.V., Jacobsen B.H., Foged N., and Sørensen K.I. 2005. Piecewise 1D Laterally Constrained Inversion of resistivity data. Geophysical Prospecting 53, 497-506.
4. Auken E., Christiansen A.V., Jacobsen L., and Sørensen K.I. 2008. A resolution study of buried valleys using laterally constrained inversion of TEM data. Journal of Applied Geophysics 65, 10-20.
5. Auken E., Christiansen A.V., Westergaard J.A., Kirkegaard C., Foged N., and Viezzoli A. 2009. An integrated processing scheme for high-resolution airborne electromagnetic surveys, the SkyTEM system. Exploration Geophysics 40, 184-192.
6. Behroozmand A.A., Auken E., Fiandaca G., and Christiansen A.V. 2012a. Improvement in MRS parameter estimation by joint and laterally constrained inversion of MRS and TEM data. Geophysics 74, WB191-WB200.
7. Behroozmand A.A., Auken E., Fiandaca G., and Christiansen A.V., and Christensen N.B. 2012b. Efficient full decay inversion of MRS data with a stretched-exponential approximation of the inline image T_2^* distribution. Geophysical Journal International 190, 900-912.
8. Blaschek R., Hördt A., and Kemna A. 2008. A new sensitivity-controlled focusing regularization scheme for the inversion of induced polarization data based on the minimum gradient support. Geophysics 73, F45-F54.

9. Brodie R. 2010. Holistic Inversion of Airborne Electromagnetic Data. PhD thesis, The Australian National University, Canberra, Australia.

10. Brodie R. and Sambridge M. 2006. A holistic approach to inversion of frequency-domain airborne EM data. Geophysics 71, G301-G312.

11. Christensen N.B. and Tølbøll R.J. 2009. A lateral model parameter correlation procedure for one-dimensional inverse modelling. Geophysical Prospecting 57, 919-929.

12. Christiansen A.V. and Auken E. 2012. A global measure for depth of investigation. Geophysics 77, WB171-WB177.

13. Constable S.C., Parker R.L., and Constable C.G. 1987. Occam's inversion: A practical algorithm for generating smooth models from electromagnetic sounding data. Geophysics 52, 289-300.

14. Cox L.H., Wilson G.A., and Zhdanov M.S. 2010. 3D inversion of airborne electromagnetic data using a moving footprint. Exploration Geophysics 41, 250-259.

15. Fiandaca G., Auken E., Gazoty A., and Christiansen A.V. 2012. Time-domain induced polarization: Full-decay forward modeling and 1D laterally constrained inversion of Cole-Cole parameters. Geophysics 77, E213-E225.

16. Fiandaca G., Ramm J., Binley A., Gazoty A., Christiansen A.V., and Auken E. 2013. Resolving spectral information from time domain induced polarization data through 2-D inversion. Geophysical Journal International, 192, 631-646.

17. Guillemoteau J., Sailhac P., and Behaegel M. 2012. Fast approximate 2D inversion of airborne TEM data: Born approximation and empirical approach. Geophys. 77, WB89-WB97.

18. Haber E., Oldenburg D.W., and Shekhtman R. 2007. Inversion of time domain three-dimensional electromagnetic data. Geophysical Journal International 171, 550-564.

19. Harbo M.S., Pedersen J., Johnsen R., and Petersen K. 2011. Groundwater in a Future Climate.

20. Jørgensen F., Scheer W., Thomson S., Sonnenborg T.O., Hinsby K., Wiederhold H., Schamper C., Burschil T., Roth.B., Kirsch R., and Auken E. 2012. Transboundary geophysical mapping of geological elements and salinity distribution critical for the assessment of future sea water intrusion in response to sea level rise. Hydrology and Earth System Sciences 16, 1845-1862.

21. Marquart D. 1963. An Algorithm for Least Squares Estimation of Nonlinear Parameters. SIAM, Journal of Applied Mathematics 11, 431-441.

22. Monteiro Santos F.A. 2004. 1-D laterally constrained inversion of EM34 profiling data. Journal of Applied Geophysics 56, 123-134.

23. Newman G. and Commer M. 2005. New advances in three dimensional transient electromagnetic inversion. Geophysical Journal International 160, 5-32.

24. Newman G.A., Anderson W.L., and Hohmann G.W. 1987. Interpretation of transient electromagnetic soundings over three-dimensional structures for the central-loop configuration. Geophysical Journal Of The Royal Astronomical Society 89, 889-914.

25. Pagliara G. and Vignoli G. 2006. Focusing inversion techniques applied to electrical resistance tomography in an experimental tank. International Association for Mathematical Geology XI International Congress Processing.

26. Portniaguine O. and Zhdanov M.S. 1999. Focusing geophysical inversion images. Geophysics 64, 874-887.

27. Sasaki Y. 2001. Full 3-D inversion of electromagnetic data on PC. Journal of Applied Geophysics 46, 45-54.

28. Sasaki Y.N.H. 2003. Topographic effects in frequency-domain helicopterborne electromagnetics. Exploration Geophysics 34, 24-28.

29. Sengpiel K.P. and Siemon B. 2000. Advanced inversion methods for airborne electromagnetic exploration. Geophysics 65, 1983-1992.

30. Sørensen K.I. and Auken E. 2004. SkyTEM - A new high-resolution helicopter transient electromagnetic system. Exploration Geophysics 35, 191-199.

31. Tikhonov A.N. and Arsenin Y.V. 1977. Solution of ill-posed problems. Winston & Sons. ISBN 0-470-99124-0.

32. Triantafilis J. and Monteiro Santos F.A. 2009. 2-dimensional soil and vadose zone representation using an EM38 and EM34 and a laterally constrained inversion model. Australian Journal of Soil Research 47, 809-820.

33. Vallée M.A. and Smith R.S. 2009. Inversion of airborne time-domain electromagnetic data to a 1D structure using lateral constraints. Near Surface Geophysics 7, 63-71.

34. Viezzoli A., Christiansen A.V., Auken E., and Sørensen K.I. 2008. Quasi-3D modeling of airborne TEM data by Spatially Constrained Inversion. Geophysics 73, F105-F113.

35. Viezzoli A., Munday T., Auken E., and Christiansen A.V. 2010. Accurate quasi 3D versus practical full 3D inversion of AEM data - the Bookpurnong case study. Preview 149, 23-31.

36. Vignoli G. and Cassiani G. 2010. Identification of lateral discontinuities via multi-offset phase analysis of surface wave data. Geophysical Prospecting 58, 389-413.

37. Vignoli G., Cassiani G., and Deiana R. 2012. Focused inversion of vertical radar profile (VRP) traveltime data. Geophysics 77, H9-H18.

38. Vignoli G., Strobbia C., Cassiani G., and Vermeer P. 2011. Statistical multi-offset phase analysis (sMOPA) for surface wave processing in laterally varying media. Geophysics 76, U1-U11.

39. Wilson G.A., Raiche A., and Sugeng F. 2006. 2.5D inversion of airborne electromagnetic data. Exploration Geophysics 37, 363-371.

40. Wisén R. and Christiansen A.V. 2005. Laterally and Mutually Constrained Inversion of Surface Wave Seismic Data and Resistivity Data. Journal of Environmental & Engineering Geophysics 10, 251-262.

41. Yang D. and Oldenburg D.W. 2012. Three-dimensional inversion of airborne time-domain electromagnetic data with applications to a porphyry deposit. Geophysics 77, B23-B34.

42. Zhdanov M.S. 2002. Geophysical inverse theory and regularization problems. Elsevier. ISBN-10: 0-444-51089-3.

43. Zhdanov M.S. and Tolstaya E. 2004. Minimum support nonlinear parametrization in the solution of a 3D magnetotelluric inverse problem. Inverse Problems 20, 937-952.

44. Zhdanov M.S., Vignoli G., and Ueda T. 2006. Sharp boundary inversion in crosswell traveltime tomography. Journal of Geophysics and Engineering 3, 122-134.